

**Vibrational electron energy loss spectroscopy in truncated dielectric slabs**Andrea Konečná,<sup>1</sup> Kartik Venkatraman,<sup>2</sup> Katia March,<sup>3</sup> Peter A. Crozier,<sup>2</sup> Rainer Hillenbrand,<sup>4</sup>  
Peter Rez,<sup>5</sup> and Javier Aizpurua<sup>1,6,\*</sup><sup>1</sup>*Materials Physics Center, CSIC-UPV/EHU, 20018 Donostia-San Sebastián, Spain*<sup>2</sup>*School for Engineering of Matter, Transport and Energy, Arizona State University, Tempe, Arizona 85287, USA*<sup>3</sup>*Eyring Materials Center, Arizona State University, Tempe, Arizona 85287, USA*<sup>4</sup>*CIC NanoGUNE and UPV/EHU, 20018 Donostia-San Sebastián, Spain  
and IKERBASQUE, Basque Foundation for Science, 48013 Bilbao, Spain*<sup>5</sup>*Department of Physics, Arizona State University, Tempe, Arizona 85287, USA*<sup>6</sup>*Donostia International Physics Center DIPC, 20018 Donostia-San Sebastián, Spain*

(Received 24 August 2018; revised manuscript received 24 October 2018; published 13 November 2018)

Specially designed instrumentation for electron energy loss spectroscopy (EELS) in a scanning transmission electron microscope makes it possible to probe very low-loss excitations in matter with a focused electron beam. Here we study the nanoscale interaction of fast electrons with optical phonon modes in silica. In particular, we analyze the spatial dependence of EEL spectra in two geometrical arrangements: a free-standing truncated slab of silica and a slab with a junction between silica and silicon. In both cases, we identify different loss channels, involving polaritonic and nonpolaritonic contributions to the total electron energy loss, and we obtain the corresponding energy-filtered maps. Furthermore, we present a comparison of the theoretical simulations for a silica-silicon junction with experimental results, and we discuss the spatial resolution attainable from the energy-filtered map considering optical phonon excitations in a conventional experimental arrangement.

DOI: [10.1103/PhysRevB.98.205409](https://doi.org/10.1103/PhysRevB.98.205409)**I. INTRODUCTION**

Recent instrumentation advances in electron energy loss spectroscopy (EELS) in the scanning transmission electron microscope (STEM) [1] have made it possible to record energy losses in the infrared (IR) energy range [2]. These developments have stimulated both experimental and theoretical investigations of the vibrational response of various organic [3–5] and inorganic [6–10] compounds probed locally by a tightly focused electron beam.

Despite the high spatial resolution that is routinely achieved in STEM imaging [11] as well as in core-loss EELS [12], the information in low-loss EEL spectra is usually collected from an area significantly beyond the beam focus, i.e., the beam interacts via the electromagnetic (EM) field with sample areas that are far away from the actual beam position [13,14]. Unless direct impact scattering (when the beam can interact with both optical and acoustic lattice vibrations [7,15,16]) takes place, most of the EEL vibrational signal arises purely from the excitation of optical phonons. The energy-filtered EEL signal corresponding to optical phonon losses enables us to achieve (sub)nanometric spatial resolution only if electrons scattered through significant angles are collected [6,17–20]. Otherwise, the spatial resolution in EEL related to the excitation of dipole-carrying optical phonon modes is typically tens of nanometers [2,8,21], given by the spatial decay of the EM field accompanying the fast electron and the EM field induced in the sample. On the other hand,

the spatial extent of the near-field beam-sample interaction is useful for recording EEL spectra in “aloof” geometry, with the electron probe outside the sample. In such an arrangement, one can avoid radiation damage caused by direct electron beam penetration, which is especially crucial for organic and other radiation sensitive samples [3,10,22,23].

The long-range interaction contributing to the EEL signal can be even more pronounced, when the beam interacts with samples supporting collective polaritonic excitations, such as plasmons or optical phonons strongly coupled with electromagnetic waves (volume and surface plasmon polaritons and phonon polaritons, respectively [24,25]). Analogously to EELS studies of plasmon polariton excitations in the visible spectral range [26–30], spatially resolved EELS characterization of propagating [8] or localized [7] phonon polaritons has been recently performed in the IR spectral range, showing a slow spatial intensity decay of polaritonic losses as a function of the electron beam distance to the sample. Moreover, similarly to plasmon polaritons, the energy and the electromagnetic near-field associated with phonon polariton excitations strongly depend on the geometry of the sample and on the electron beam position. First experimental and theoretical studies on phonon polaritons showed that it is usually necessary to perform numerical calculations or develop analytical models in order to fully understand EEL spectral features, as well as the spatial dependence of the signal [7,8,31,32].

In this paper, we calculate the spatial dependence of EEL spectra for an electron beam scanned across a truncated slab and a slab with a junction between two materials. We focus on a truncated thin slab of silica (SiO<sub>2</sub>), and in particular

\*aizpurua@ehu.es

on the emergence of both polaritonic and nonpolaritonic optical phonon excitations in the region between 90 and 160 meV. Then we analyze the EEL spectra at a silica-silicon interface. Such geometrical arrangements are very common in experimental situations and represent benchmarks to test the spatial resolution of energy-filtered EELS. Furthermore, thin oxide layers grown on silicon substrates [33] are of high interest in the semiconductor industry, and in particular amorphous silica is often exploited as an insulating material in electronic nanodevices due to its high dielectric strength [34,35]. Spatial characterization of the vibrational response together with high-resolution imaging using STEM-EELS could help better understand heat dissipation in such nanostructures.

In our calculations, we adopt a theoretical framework based on the linear dielectric response, successfully applied in the analysis of valence EELS [36,37]. We note that this theoretical approach works in the regime of low-momentum scattering and disregards the possibility of acoustic mode excitation. We first present analytical models to describe an infinite interface and an extended thin slab that help to understand the results from numerical simulations. We identify different types of losses arising for both sample geometries and discuss the spatial dependence of the energy-filtered line scans. Moreover, for the silica-silicon junction, we demonstrate excellent agreement between the simulated spectra and experimental data [21].

## II. CLASSICAL DIELECTRIC RESPONSE THEORY

EELS of low-loss valence and vibrational excitations can be modeled using classical electrodynamics where the sample geometry and the local dielectric properties  $\varepsilon(\mathbf{r}, \omega)$  determine the response of the system. The electron energy loss  $\Delta E$  can be calculated as the work  $W$  of the induced electromagnetic field  $\mathbf{E}^{\text{ind}}$  coming from the beam-sample interaction against the fast-moving electron [13,26],

$$\Delta E = -W = e \int d\mathbf{r}_e \cdot \mathbf{E}^{\text{ind}}(\mathbf{r}_e, t), \quad (1)$$

where the work is integrated along the electron trajectory  $\mathbf{r}_e(t)$ ,  $e$  is the elementary charge, and  $t$  stands for time. If we neglect the electron beam recoil, which is well justified for fast electrons [38], we have  $\mathbf{r}_e(t) = (b, 0, vt)$  for an electron moving at speed  $v$  in the  $z$  direction. The electron energy loss probability  $\Gamma(\omega)$  of losing energy  $\hbar\omega$ , which represents the EEL spectrum, is defined as  $\Delta E = \int_0^\infty d\omega \hbar\omega \Gamma(\omega)$ , yielding [13]

$$\Gamma(\omega, b) = \frac{e}{\pi \hbar \omega} \int_{-\infty}^{\infty} dz \operatorname{Re} \left\{ E_z^{\text{ind}}(\mathbf{r}_e(t), \omega) \exp\left(-\frac{i\omega z}{v}\right) \right\}. \quad (2)$$

Hence, to calculate the EEL probability, one needs to know the  $z$  component of the induced electric field along the electron trajectory. Maxwell's equations can be solved analytically for several simple geometrical arrangements, including an electron moving in an infinite medium [13], along infinite interfaces [30,39], or penetrating through infinite slabs [26,40–42]. Although in more complex geometries the solution has to be obtained numerically, it is often possible to understand

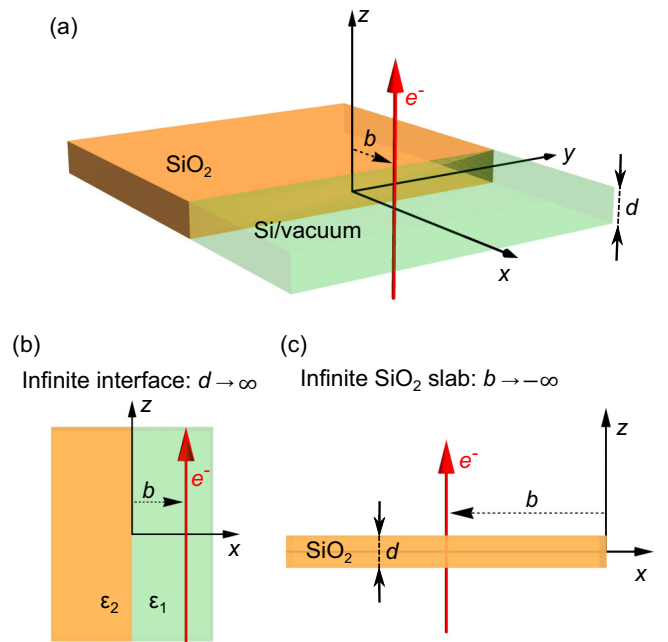


FIG. 1. (a) Schematics of the considered geometry. The sample is a slab of thickness  $d$  infinite in the  $xy$  plane with a sharp interface in the plane  $x = 0$ . We consider either a slab with a silica-silicon interface or a semi-infinite silica slab surrounded by vacuum. A 60-keV electron ( $v = 0.446c$ ) is moving in the positive  $z$  direction at the distance  $b$  from the silica-silicon or silica-vacuum interface at  $x = 0$ . Negative values of  $b$  stand for the beam inside silica. Considered limiting cases of (b) an infinite interface geometry and (c) an infinite silica slab.

EEL spectral features by considering limiting geometrical cases that are solved analytically. For our geometry of interest, sketched in Fig. 1(a), we will thus start from the solutions of the response of an infinite interface [Fig. 1(b)] and an infinite silica slab [Fig. 1(c)].

### A. Infinite interface geometry

If we disregard for now the presence of the slab top and bottom surfaces, the situation would correspond to the electron moving parallel to an infinite interface between two media as sketched in Fig. 1(b). For a beam in a medium characterized by a local dielectric function  $\varepsilon_1(\omega)$  passing at an impact parameter  $b$  from a neighboring medium characterized by a dielectric function  $\varepsilon_2(\omega)$ , the EEL probability  $\Gamma_{\text{interface}}$  including retardation effects can be expressed as [30]

$$\Gamma_{\text{interface}} = \frac{2de^2}{4\pi^2 \varepsilon_0 \hbar v^2} \int_0^{q_y^c} dq_y \operatorname{Im} \left\{ \underbrace{-\frac{1 - \varepsilon_1 \beta^2}{\varepsilon_1 \alpha_1}}_{\text{bulk}} + e^{-2\alpha_1 |b|} \times \left( \underbrace{\frac{1 - \varepsilon_1 \beta^2}{\varepsilon_1 \alpha_1}}_{\text{Begr.}} - \underbrace{\frac{2}{\varepsilon_1 \alpha_2 + \varepsilon_2 \alpha_1} + \frac{2\beta^2}{\alpha_1 + \alpha_2}}_{\text{interface}} \right) \right\}, \quad (3)$$

where  $\epsilon_0$  is the vacuum permittivity,  $\beta = v/c$ ,  $c$  is the speed of light in vacuum,  $\alpha_{1/2} = \sqrt{(\omega/v)^2 + q_y^2} - \epsilon_{1/2}\omega^2/c^2$ , and  $\hbar q_y$  is the  $y$  component of the momentum. The integration above is performed up to the cutoff  $q_y^c$  to prevent divergence of the integral for  $q_y \rightarrow \infty$ .<sup>1</sup>

The nonretarded version of Eq. (3),  $\Gamma_{\text{interface}}^{\text{NR}}$ , is obtained by letting  $c \rightarrow \infty$ :

$$\Gamma_{\text{interface}}^{\text{NR}} = \frac{2de^2}{4\pi^2\epsilon_0\hbar v^2} \text{Im} \left\{ \underbrace{\frac{\ln(2q_y^c v/\omega)}{\epsilon_1}}_{\text{bulk}} + K_0\left(\frac{2\omega b}{v}\right) \left( \underbrace{\frac{1}{\epsilon_1}}_{\text{Begr.}} - \underbrace{\frac{2}{\epsilon_1 + \epsilon_2}}_{\text{interface}} \right) \right\}, \quad (4)$$

where  $K_0(x)$  stands for the zero-order modified Bessel function of the second kind. The bulk losses were integrated up to the momentum cutoff, assuming  $q_y^c \gg \omega/v$ , whereas the integrals of the remaining loss terms were carried out up to  $q_y^c \rightarrow \infty$ . We also implicitly consider  $q_x^c \rightarrow \infty$ . We note that the classical description using the local dielectric function is valid only for small scattering angles, where the  $q_{x,y}$  wave numbers are smaller than the inverse of the atomic distances of the materials [40], which is in principle not fully fulfilled for both  $\Gamma_{\text{interface}}^{\text{NR}}$  and  $\Gamma_{\text{interface}}$ . Nevertheless, we analyze here the EELS of optical phonons whose dominant contribution is at low momenta [8], thus justifying the expressions above. Only if we aim at properly describing momentum-filtered experiments or interaction with acoustic phonons would it be necessary to consider the dispersion of the sample's response and a full description of the phononic density of states [6,15,16,20,43].

We discuss now the different loss contributions in Eqs. (3) and (4). We denote the bulk loss as if the electron were traveling across an infinite medium characterized by  $\epsilon_1(\omega)$ . Notice that the (nonretarded) bulk loss function  $\text{Im}[-1/\epsilon_1]$  has a pole if  $\epsilon_1(\omega_b) = 0$ . This condition is satisfied for silica in the IR, as observed in Fig. 2(a), where  $\text{Re}[\epsilon_{\text{SiO}_2}]$  (blue line; also see the corresponding label) is plotted with dielectric data obtained from Ref. [44]. For energies above 132 meV, silica exhibits a Si-O-Si asymmetric stretching mode with a large effective charge (dipole strength) [45,46], which yields a negative real part of the dielectric response in the shaded region, where it enables excitation of surface phonon polaritons, as in polar crystals [7,8,24].  $\text{Re}[\epsilon_{\text{SiO}_2}]$  is negative almost up to the bulk, longitudinal-optical (LO) phonon mode energy  $\hbar\omega_{\text{SiO}_2,b} = 154$  meV, where we observe an intense peak in the nonretarded bulk loss function  $\text{Im}[-1/\epsilon_{\text{SiO}_2}]$ , shown by the dashed black curve in Fig. 2(b). Another spectral feature appears due to the Si-O-Si symmetric stretch at about 100 meV [45,46]. However, the corresponding effective charge is relatively small and there is no pole of  $\epsilon_{\text{SiO}_2}$  around this region ( $\text{Re}[\epsilon_{\text{SiO}_2}] > 0$ ). The symmetric stretching mode

<sup>1</sup>See Ref. [30] for expressions taking into account the circular collection aperture.

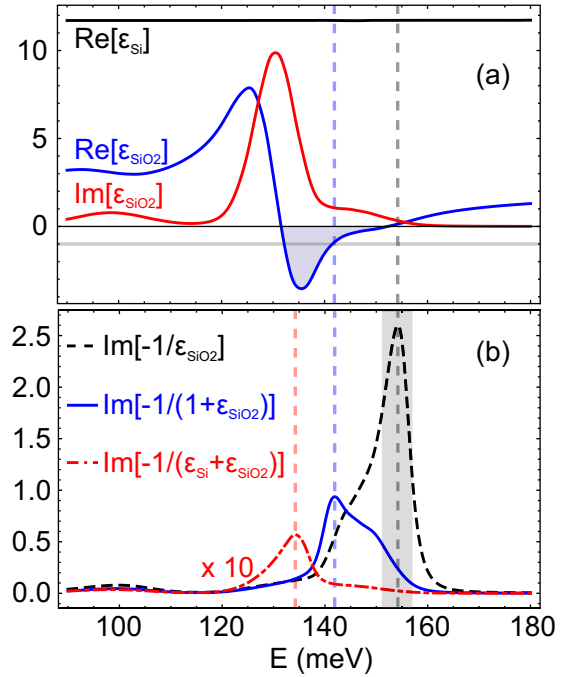


FIG. 2. (a) Real and imaginary parts of the dielectric function of silica  $\epsilon_{\text{SiO}_2}$  together with the real part of the dielectric function of silicon (the imaginary part is four orders of magnitude smaller and thus negligible). (b) Bulk loss function of silica  $\text{Im}[-1/\epsilon_{\text{SiO}_2}]$  (dashed black curve) with peak energy at 154 meV, the silica-vacuum interface loss function  $\text{Im}[-1/(\epsilon_{\text{SiO}_2} + 1)]$  peaking at 142 meV (solid blue curve) and a much weaker silica-silicon interface loss function  $\text{Im}[-1/(\epsilon_{\text{Si}} + \epsilon_{\text{SiO}_2})]$  with the maximum at 134 meV (dashed-dotted red curve). Vertical dashed lines mark the corresponding positions of the loss peaks. The gray shaded area in (b) emphasizes the region of bulk losses in  $\text{SiO}_2$ .

thus contributes only weakly to the bulk loss and does not promote polaritonic excitations.

The interface loss function  $\Gamma_{\text{interface}}$  also contains the so-called “Begrenzungs-effekt” contribution, which is responsible for a reduction of the bulk losses. It has the same functional dependence as the bulk loss except for the negative sign and the prefactor that increases for small impact parameters  $b$ . Therefore, for a close approach of the electron to the interface, this contribution almost perfectly compensates for the bulk loss. The “pure” interface losses will become dominant in such a situation. In the nonretarded case, the pole of the interface loss function  $\text{Im}[-1/(\epsilon_1 + \epsilon_2)]$  would be at an energy where  $\epsilon_1(\omega_s) + \epsilon_2(\omega_s) = 0$ . As  $\text{Re}[\epsilon_{\text{SiO}_2}] < 0$  and  $|\text{Re}[\epsilon_{\text{SiO}_2}]| > \text{Re}[\epsilon_{\text{vac}}] = 1$ , this condition is approximately fulfilled for the silica-vacuum interface [solid blue curve in Fig. 2(b) peaking at  $\hbar\omega_{\text{SiO}_2/\text{vac},s} = 142$  meV]. The silica-vacuum interface thus supports the excitation of surface phonon polaritons. This is not possible at the silica-silicon interface because of the large and almost constant real value of the dielectric function of silicon in the spectral region of interest (plotted by the black line in Fig. 2(a), data taken from Ref. [47]). As we have  $|\text{Re}[\epsilon_{\text{SiO}_2}]| < \text{Re}[\epsilon_{\text{Si}}] \sim 11.7$ , the silica-silicon interface loss function  $\text{Im}[-1/(\epsilon_{\text{Si}} + \epsilon_{\text{SiO}_2})]$  exhibits only a weak nonresonant peak at 134 meV (dashed-dotted red curve in Fig. 2(b) multiplied by factor of 10).

### B. Infinite slab geometry

If we place the beam far from the interface at  $x = 0$  in Fig. 1(a), i.e.,  $b \rightarrow \pm\infty$ , the geometrical arrangement will be well described as if the beam were passing through a slab infinite in the  $xy$  plane. Due to the possibility of exciting surface phonon polaritons at the silica-vacuum interface, we are particularly interested in such a calculation for the infinite silica slab as sketched in Fig. 1(c). In the nonretarded approximation, the slab loss probability can be expressed in a compact form (for the retarded expressions, see Refs. [40,42]) as

$$\Gamma_{\text{slab}}^{\text{NR}} = \underbrace{\frac{de^2}{4\pi^2\epsilon_0\hbar v^2} \text{Im}\left\{-\frac{1}{\epsilon_{\text{SiO}_2}}\right\} \ln\left(\frac{Q_c^2 v^2 + \omega^2}{\omega^2}\right)}_{\text{bulk}} + \frac{e^2 v^2}{\epsilon_0 \pi^2 \hbar} \int_0^{Q_c} dQ \text{Im}\left\{\frac{Q^2(\epsilon_{\text{SiO}_2} - 1)^2}{(Q^2 v^2 + \omega^2)^2 \epsilon_{\text{SiO}_2}} \times \left[ \underbrace{\frac{\sin^2(\frac{\omega d}{v})}{\epsilon_{\text{SiO}_2} + \tanh(dQ)}}_{\text{sym.}} + \underbrace{\frac{\cos^2(\frac{\omega d}{v})}{\epsilon_{\text{SiO}_2} + \coth(dQ)}}_{\text{antisym.}} \right] \right\}, \quad (5)$$

Begr. +coupled surf.

where  $Q = \sqrt{q_x^2 + q_y^2}$  is the wave number in the perpendicular direction with respect to the electron trajectory, and  $\hbar Q_c$  stands for the perpendicular momentum cutoff. Unfortunately, for the complex dielectric function  $\epsilon_{\text{SiO}_2}$  and an arbitrary slab thickness, it is not possible to solve the integral in Eq. (5) in closed form, and the integration has to be performed numerically.

The loss probability (5) also contains several loss channels: the bulk loss probability, which would correspond to the losses of the beam in an infinite medium (but now integrated over the perpendicular momentum taking account of the cylindrical symmetry), and the remaining loss term arising due to the presence of the top and bottom slab surfaces. The latter will have strong effects on the resulting spectra, especially in the case of polaritonic materials. For thin slabs, the bulk loss will be reduced by the negative Begrenzungs contribution, and importantly, the upper and bottom surfaces become electromagnetically coupled, giving rise to symmetric and antisymmetric coupled surface modes [48].

We note that the integrand of Eq. (5) can be understood as a dispersion of these modes, taking into account the coupling with the field of the fast electron [8]. In particular, the fast electron excites efficiently the charge-symmetric coupled surface modes [see the term marked as “sym.” in the last factor of Eq. (5)] [31,49–51], whose electron-excitation weighted dispersion we observe in Figs. 3(a) and 3(b). To see the dependence on the slab thickness, we evaluate the integrand for a silica slab with thickness  $d = 10$  and 100 nm, respectively. Notice that the optimum of the coupling between the fast electron and the slab modes shifts to higher energies for thicker slabs, which can be seen from an analysis of the last line of Eq. (5). The surface coupling can be neglected for thick slabs ( $d \gtrsim 300$  nm for 60-keV electrons and silica), where the electron would excite independent surface phonon polaritons (yielding the loss peak approximately at an energy

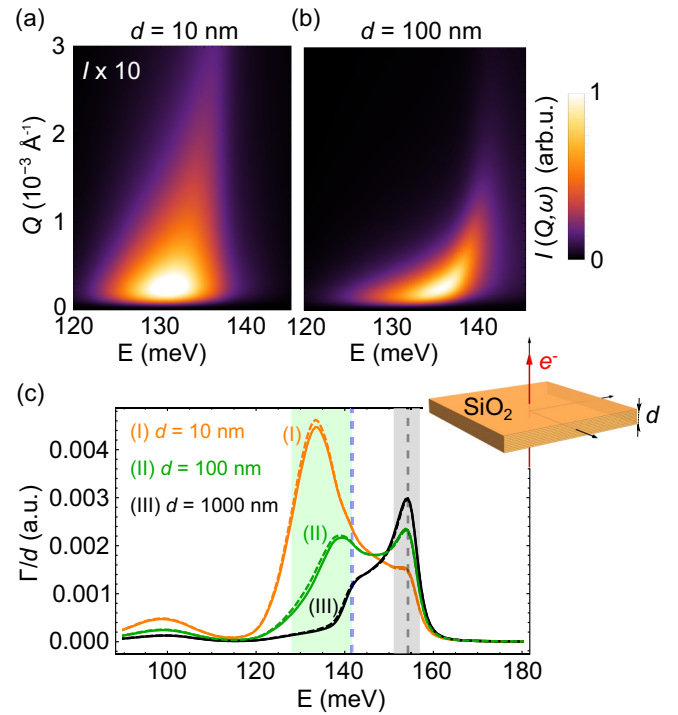


FIG. 3. (a,b) Integrands of Eq. (5) evaluated for a 60-keV electron beam passing through an infinite silica slab of thicknesses 10 and 100 nm, respectively. For better visualization, the magnitude of (a) was multiplied by 10. (c) The nonretarded [full lines, according to Eq. (5)] and retarded (dashed lines) loss probability divided by the slab thickness, evaluated for  $d = 10/100/1000$  nm as denoted in the plot. The momentum cutoff used in the calculation is  $Q_c = 0.27 \text{ \AA}^{-1}$ .

given by the condition  $\epsilon_{\text{SiO}_2} + 1 = 0$ ) at the top and bottom slab surfaces. However, the surface loss for very thick slabs will be overwhelmed by the bulk loss.

The calculated loss probability spectra for a silica slab with different thicknesses are depicted in Fig. 3(c). We compare the nonretarded calculation using Eq. (5) (full lines) with the fully retarded solution (dashed lines) for 60-keV electron beam excitation. The retardation effects in this case introduce only a small redshift as expected and a slight broadening of the peaks. In the calculated spectra, we observe three peaks: a weak peak close to 100 meV coming from excitation of the symmetric stretch of silica, the peaks in the light-green area can be assigned to the coupled-surface polaritonic type of loss, and finally the bulk loss contribution close to  $\hbar\omega_{\text{SiO}_2,b} = 154$  meV (light gray area).

The slab thickness determines the relative intensity of the bulk and coupled-surface losses, as well as the spectral position of the loss peak due to the symmetric coupled-surface mode [8], which we could anticipate from Figs. 3(a) and 3(b). The peak energy  $\hbar\omega_M$  can be found analytically from Eq. (5) for thin slabs of materials with small damping ( $\text{Im}[\epsilon] \approx 0$ ). The maximum is then given by the condition  $\sqrt{3}\omega_M d = v \ln\{[\epsilon(\omega_M) - 1]/[\epsilon(\omega_M) + 1]\}$  [40], which, however, holds only approximately for thin silica slabs as  $\text{Im}[\epsilon_{\text{SiO}_2}]$  is not negligible. The thicker the slab is, the closer the peak appears to the silica-vacuum surface phonon energy at 142 meV (for

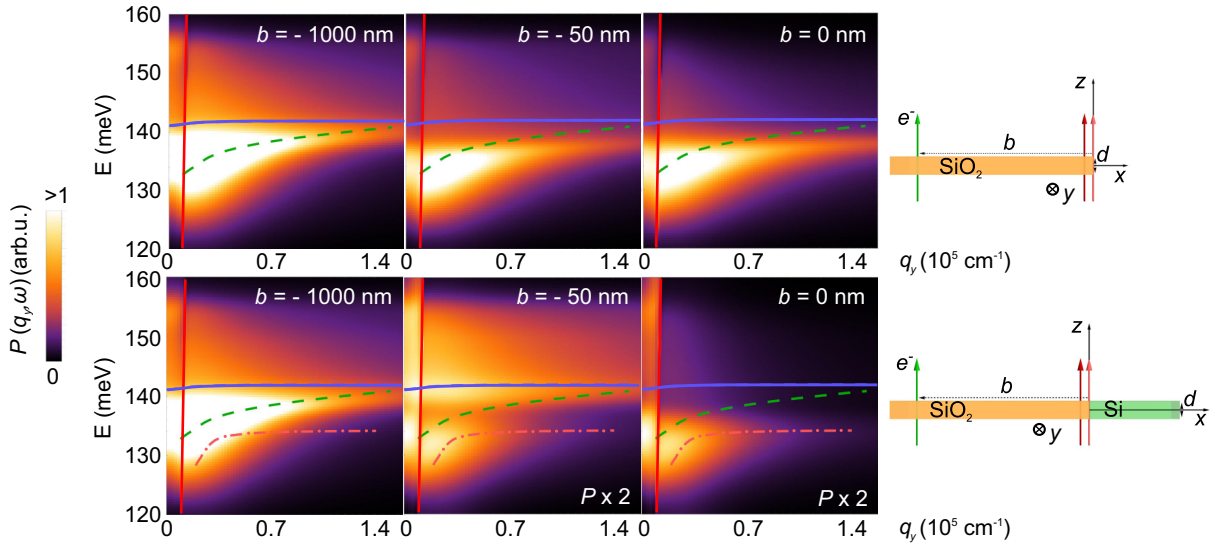


FIG. 4. Numerically calculated momentum-resolved EEL probability  $P(q_y, \omega)$  for a truncated silica slab (upper row) and a silica-silicon junction (lower row) for two impact parameters of the beam passing through silica ( $b = -1000$  and  $-50$  nm, respectively) and another impact parameter at the slab truncation or junction ( $b = 0$  nm). The slab thickness is  $d = 100$  nm. The intensity of the last two plots for the silica-silicon junction is multiplied by a factor of 2. The overlaying curves are analytically calculated maxima of momentum-dependent loss probabilities for the infinite silica slab (dashed green), the infinite silica-vacuum interface (solid blue), and the infinite silica-silicon interface (dashed-dotted red). Solid straight red lines denote the threshold for radiation losses.

$d = 1000$  nm hidden in the “shoulder” of the bulk loss).<sup>2</sup> On the other hand, the weak nonpolaritonic loss at 99 meV, which does not experience any substantial influence of the slab surface coupling, stays at the same spectral position for all slab thicknesses.

### III. VIBRATIONAL EELS AT A TRUNCATED SILICA SLAB AND AT A SILICA-SILICON SLAB JUNCTION

We address now a highly interesting situation in experiments, namely a truncated silica slab and a slab with a silica-silicon junction. We have implemented numerical EELS calculations in the commercial software COMSOL MULTIPHYSICS, which employs a finite-element method to numerically solve Maxwell’s equations (see Appendix A for details). We focus on the spectral region of the asymmetric Si-O-Si stretch, where we can expect polaritonic behavior of silica. We define the momentum-dependent loss probability  $P(q_y, \omega)$ , which is related to the total loss probability as

$$\Gamma(\omega) = \int_0^{q_y^c} dq_y P(q_y, \omega), \quad (6)$$

and is obtained by considering the 2D geometry sketched in Fig. 4. In the simulation, we vary the out-of-plane wave vector  $q_y$  [8] so that we enable propagation of a wave  $\mathbf{E}(x, y, z) = \tilde{\mathbf{E}}(x, z)\exp(iq_y y)$  and obtain the momentum-resolved spectra with a discrete step  $\Delta q_y$ .

<sup>2</sup>If the imaginary part (damping) of  $\epsilon_{\text{SiO}_2}$  were smaller, we would observe two separate peaks in the green region: the first corresponding to the charge-symmetric slab mode, and another peak at the silica-vacuum surface phonon energy ( $\epsilon_{\text{SiO}_2} + 1 = 0$  at 142 meV) [40].

The calculated momentum-resolved spectra for the slab thickness  $d = 100$  nm are shown in the color plots of Fig. 4, and they can again be understood as dispersion relationships obtained by taking into account the coupling with the field of the fast electron, similarly to the expressions in the integrals of Eqs. (3) and (5) [the latter evaluated in Figs. 3(a) and 3(b)]. The green dashed line in Fig. 4 shows the maxima extracted from Fig. 3(b), tracing the dispersion of the charge-symmetric coupled-surface mode. The solid blue and dashed-dotted light red lines trace the maxima of the momentum-dependent retarded loss in the integrand of Eq. (3) at an infinite silica-vacuum and a silica-silicon interface, respectively.

From the plots for the impact parameter  $b = -1000$  nm, it is clearly noticeable that the situation is close to the infinite silica slab limit as the numerical result nicely matches the symmetric coupled-surface mode dispersion (green dashed curve). A smaller contribution of the bulk loss appears at higher energies around 155 meV, which becomes the dominant loss channel for higher momenta ( $q_y \gtrsim 0.01 \text{ \AA}^{-1}$ , not shown in the plots).

For smaller impact parameters ( $|b| \lesssim 100$  nm; with  $b$  negative), the results differ from the infinite silica slab limit. For the silica truncated slab, we observe an intense excitation of a mode with a different dispersion. We assign this mode to the coupled edge mode, with limiting energy  $\hbar\omega_{\text{SiO}_2, \text{edge}} = 140$  meV for  $q_y \rightarrow \infty$ , which is slightly lower than the silica-vacuum interface loss limit  $\hbar\omega_{\text{SiO}_2/\text{vac}, s}$ . We note that the coupled edge dispersion cannot be reproduced analytically [36].

On the other hand, the momentum-resolved probability when the electron beam is at the silica-silicon junction ( $b = 0$  nm, bottom plot) resembles the dispersion of the silica-silicon infinite interface (marked by the dashed-dotted light red curve). Compared to the vacuum-surrounded silica truncated slab, the coupled edge modes cannot be excited in the

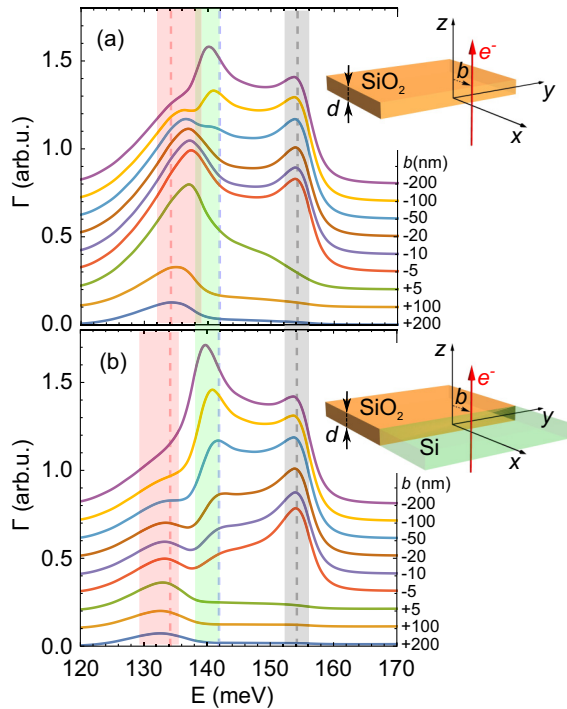


FIG. 5. Numerically calculated EEL spectra for an electron beam probing (a) a truncated silica slab and (b) a silica-silicon junction at varying impact parameter  $b$  as displayed in the insets.  $b$  is negative when the beam is inside silica and positive when it is placed either in vacuum or in silicon. The slab thickness is in both cases  $d = 100$  nm. Spectra are vertically shifted by a constant value for clarity.

$\text{SiO}_2/\text{Si}$  junction due to the presence of the high refractive index silicon at one of the interfaces. If the beam is slightly moved from the interface into the silica ( $b = -50$  nm, bottom plot), we observe both the interface loss and also an additional loss contribution around 140 meV. In this case, the beam excites the coupled surface modes across the silica slab that are influenced by the presence of silicon and can get reflected at the interface. In particular, when the beam is very close to the junction, the constructive interference of the reflected waves and those propagating toward the interface (with short-wavelength polaritons dominantly involved) determines the position of the spectral maximum. Therefore, the coupled-surface loss appears close to the silica surface phonon energy at 142 meV, which is a large-wave-vector limit of surface phonon polariton dispersion denoted by the solid blue line.

Now we focus on conventional energy-dependent EELS. We perform numerical calculations in a 3D geometry, but as we mentioned, the results can be reproduced also from 2D calculations according to Eq. (6). We note that the finite size of the mesh elements in the numerical simulation acts as an effective momentum cutoff and thus naturally eliminates the divergence of the losses for high momenta. The average cutoff in the performed 3D simulations is  $\sim 0.2 \text{ \AA}^{-1}$ .

The spectra calculated for a varying impact parameter both from the silica-vacuum and from the silica-silicon junction are plotted in Figs. 5(a) and 5(b), respectively. The spectral sets exhibit two common features: the bulk loss peak around 154 meV (gray region) and the coupled-surface loss (green

region around 140 meV) appear when the beam is inside silica, as derived from Eq. (5). As the beam is getting closer to the interface, we observe a weakening of the coupled-surface loss peak and a slight continuous shift of its energy toward the silica surface phonon energy at  $\hbar\omega_{\text{SiO}_2/\text{vac},s} = 142$  meV (denoted by the blue dashed line), which is related to the momentum dependence discussed above.

The lowest-energy spectral features appearing in the red region correspond to a strong silica polaritonic coupled edge mode in Fig. 5(a) and to a weaker nonresonant silica-silicon junction excitation in Fig. 5(b), respectively (as revealed also in the momentum-resolved spectra of Fig. 4). The spectral shape and peak position of the latter contribution can be described by the silicon-silica interface loss function  $\text{Im}\{-1/(\epsilon_{\text{SiO}_2} + \epsilon_{\text{Si}})\}$ . We have also found that when the beam goes through silicon, a relatively strong positive background is produced in the spectra. As silicon has a large refractive index, it introduces a contribution of radiation losses to the total energy loss. Radiation losses appear above the light lines in Fig. 4 and become the dominant loss channel when the beam goes through silicon ( $b > 0$ ).

#### IV. SPATIAL VARIATION OF EEL INTENSITY

We complete our analysis by addressing the spatial variation of EEL intensity at the energies of the different excitations identified. We also compare the theoretical results with experimental observations [21].

The impact parameter dependence of the EEL signal filtered at the energies of the loss peaks of the coupled-edge, coupled-surface, and bulk losses is plotted in Fig. 6(a) for the silica truncated slab and in Fig. 6(b) for the silica-silicon slab junction. We further add the intensity of the nonpolaritonic contribution at 100 meV in (a). Due to the large damping present in the material response, it is not straightforward to separate the contributions from the different loss channels, as they spectrally overlap and are rather blurred (see, e.g., Fig. 4). However, the plots in Figs. 6(a) and 6(b) provide valuable insight.

Outside the truncated silica slab ( $b > 0$  nm), we observe that the coupled edge excitation is dominant [orange points in Fig. 6(a)]. A smaller portion of the signal at the coupled-surface loss (green squares) and at the bulk loss (black circles) arises mostly due to the spectral overlap. As the beam is scanned across the truncation ( $b \leq 0$  nm), we observe an immediate increase in the signal at the bulk loss energy, which eventually becomes constant. The bulk signal is connected with higher momentum transfer, and we note that in the case of no spectral overlap (lower losses in the material's response), the bulk signal would exhibit a steplike profile close to the interface. The coupled-surface loss probability also increases when the beam is scanned into the material (negative  $x$  direction), and, at larger distances from the truncation, similarly to the bulk loss, it becomes constant (not shown in the plot). We note that the large damping of silica hides clear spectral signatures of interference of the coupled-surface waves propagating toward and backward from the interface at  $x = 0$  [8], and the energy-filtered intensity is thus increasing smoothly. The edge-mode excitation probability shows a maximum for the beam positioned exactly at the edge

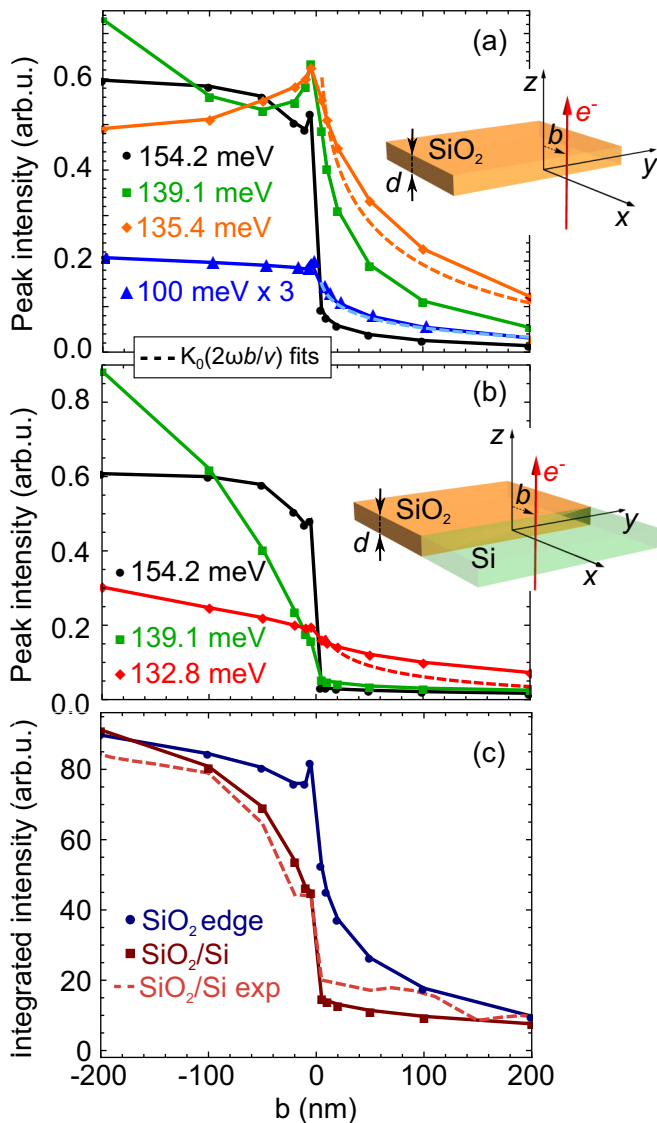


FIG. 6. Spatial dependence of EEL intensity at fixed energies calculated for a truncated silica slab (a) and at a silica-silicon junction (b). The energies correspond to the silica bulk loss peak (black circles), the coupled-surface loss for an infinite 100-nm-thick silica slab (green squares), the silica edge excitation [orange diamonds in (a)], and the nonpolaritonic Si-O-Si symmetric stretch signal [blue triangles in (a), multiplied by 3]. The spatial dependence of the silicon-silica junction excitation intensity is plotted in (b) (red diamonds). The peak intensities were obtained from spectra in Fig. 5. Dashed curves are fits of the decay for  $b > 0$  by  $K_0(2\omega b/v)$  at 100 meV (light blue line, which traces well the calculated points—triangles), at coupled-edge loss energy (orange line, which deviates from the diamonds) and junction excitation energy (red line, which deviates from the diamonds). Graph (c) depicts the total intensity integrated over an energy window of 120–160 meV for the silica edge (dark blue circles) and silica-silicon slab junction (dark red squares). Symbols represent the calculated data, lines are guides to the eye. The pink dashed line shows the experimental result for the silica-silicon junction integrated over a 120–180 meV energy window.

( $b = 0$ , orange diamonds) and smoothly decreases with the beam distance from the truncation on both sides with different decay.

We also plot the signal filtered out at 100 meV in Fig. 6(a) (blue triangles). The spectral overlap with other loss channels in this region is not that pronounced, and we can thus study the spatial dependence of this nonpolaritonic contribution. When the beam is scanned into the silica, the intensity of the 100-meV loss slightly increases and quickly saturates, similar to the bulk loss. As the influence of coupling of the silica edges and surfaces can be neglected at this energy (the excitation has nonpolaritonic character), the signal drop for the beam outside the slab approximately follows the infinite-interface decay. Indeed, a fit by the  $K_0(2\omega b/v)$  dependence [see Eq. (4)] reasonably traces the result of the numerical simulation (blue dashed curve), except for the singular behavior close to  $b = 0$ . We emphasize that the functional dependence of the signal decay strongly depends on the particular type of excitation and the corresponding induced EM field distribution. In summary, the signal decay from polaritonic materials can be approximated by the  $K_0$  dependence either for an infinite interface ( $d \rightarrow \infty$ ) or very small impact parameters ( $b \ll d$ ) in the cases when retardation effects can be neglected. As we demonstrate here,  $K_0$  fits the decay from thin truncated slabs only if the excitation is not polaritonic and is not appropriate for modeling the decay when the coupled-edge modes are involved [see the orange diamonds versus the dashed orange curve in Fig. 6(a)]. In such a case, the signal decay has to be retrieved numerically.

The spatial dependence of the energy-filtered signal changes substantially when the beam is scanned across the silica-silicon junction, as shown in Fig. 6(b). Due to the nonresonant character of the excitation at the silica-silicon interface at 132.8 meV, we observe only a tiny peak at the junction ( $b = 0$ ). The “interface” signal for  $b > 0$  comes mostly from the radiation, Čerenkov-type losses in silicon, and therefore slowly decreases with the distance of the beam to the interface (red diamonds). In this case, retardation effects (i.e., the constant radiation contribution) make the fitting of the signal decay by the  $K_0$  dependence (red dashed curve) not suitable. On the contrary, we get an immediate decrease in the bulk and the coupled-surface loss signal when the beam crosses the interface toward silicon (black circles and green squares, respectively). Importantly, the smaller spectral overlap of the loss channels and the suppression of the coupled edge excitation because of the presence of silicon make it possible to obtain nanometer spatial resolution by filtering the signal at the bulk loss or coupled-surface loss energies.

In the case of materials supporting low-loss phonon-polariton excitations (e.g., SiC or MgO), filtering the EEL signal at the LO phonon energy, which involves higher momentum transfer, should enable us to resolve material interfaces with very high resolution. Otherwise, losses in the acoustic phonon excitations or special scattering geometries can be exploited to retrieve (sub)nanometric localization of the vibrational signal.

To compare the calculated data with experiments, we need to take into account the finite instrumental resolution. For this reason, we plot the EEL intensity integrated over a wider energy window (120–160 meV) in Fig. 6(c). The integrated spectral signal corresponding to the truncated silica slab peaks at  $b = 0$  and then slowly decays for  $b > 0$  (dark blue circles). The integrated signal for the silica-silicon junction (dark red squares) exhibits a nearly steplike profile very close to the interface ( $|b| < 5$  nm) with a smooth increase when the beam is placed into the silica ( $b \leq -5$  nm) and a positive radiation background for  $b > 0$ .

In the analyzed cases, the calculations predict that it would be possible to use either the energy-filtered signal or the integrated signal (the energy-filtered signal in a larger energy range) to distinguish the edge boundary with nanometric precision. However, we expect that the peak at the boundary of the truncated silica slab ( $b = 0$ ) will be smeared out in experiments, since it arises from a perfectly abrupt interface considered in the theoretical simulations, and it also neglects the finite convergence angle of the beam. Hence, in such an arrangement, the nature of the electron-sample interaction will make it experimentally difficult to distinguish the material boundary directly from the energy-filtered maps, and thus a correlation with high-resolution imaging capabilities will be needed [2].

On the other hand, the interface between silica and silicon can be well distinguished by filtering the loss at energies of either bulk or coupled-surface losses, as they are strongly suppressed close to the junction. As these losses are prevailing in the overall spectral response, the sudden drop of intensity is also observed in the integrated signal. This is indeed confirmed by comparing the theoretical prediction with the experimentally measured data for the same geometrical arrangement [21], where the spectral intensity was integrated over a 120–180 meV energy window (for details on the experimental setup, see Appendix B). The experimental result [pink dashed curve in Fig. 6(c)] agrees reasonably well with the theoretical prediction (dark red squares). The steplike profile is still present for  $|b| < 5$  nm, and thus we can conclude that the dielectric screening by silicon helps to distinguish the interface directly from the EELS line scan.

Finally, in Fig. 7 we show a direct comparison of the experimental spectra (dashed curves) and the numerically calculated spectra from Fig. 5(b) convolved with a point spread function (PSF) to simulate the experimental resolution (solid curves) [8]. We approximate the PSF by a Gaussian function with a full width at half-maximum (FWHM) of 20 meV. Unfortunately, such resolution smears out the finer spectral structure shown in Fig. 5, and only two main peaks can be observed. We obtain very good agreement between the theory and experiment in the spectral positions and relative intensities of the peaks above 130 meV. When the beam is passing through silicon, the experimental spectra are noisier and we observe that the calculated spectra are narrower than the experimental ones. We observe that all theoretical spectra underestimate the strength of the 100-meV Si-O-Si symmetric stretch. These discrepancies can be caused by a contribution from impact scattering, the experimental noise, differences in the sample geometry, including possible mixing of materials, and the finite size of the probe. We note

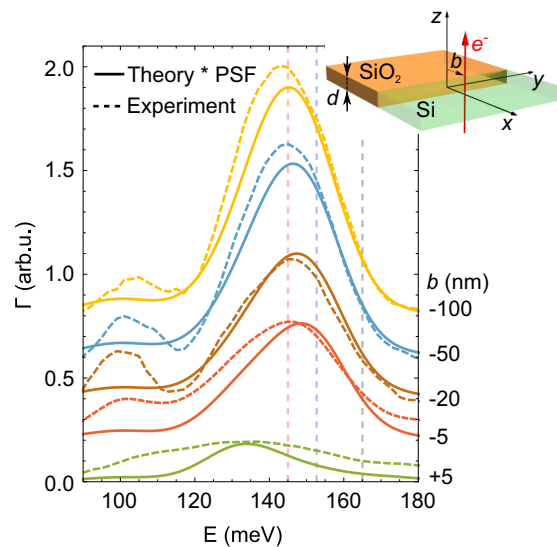


FIG. 7. Numerically calculated EEL spectra from Fig. 5 after convolution with a point spread function (PSF) represented by a Gaussian function of FWHM 20 meV mimicking the finite experimental resolution (full lines) and experimentally measured spectra (dashed lines, taken from Ref. [21]). The impact parameters as denoted next to the plot. The spectra are vertically shifted for clarity.

that a recent experimental EEL study reaching a spectral resolution of  $\sim 8$  meV [52] demonstrates very clearly the finer spectral details predicted in Fig. 5. One might expect further advances in vibrational EELS analysis along these lines in the near future with constantly improving experimental capabilities [53].

## V. SUMMARY

We have thoroughly analyzed the spatial dependence of EEL spectra for two relevant geometrical arrangements: the truncated slab of silica and the slab with an interface of silica and silicon, representing typical geometry for TEM specimens. We have observed a large contribution to EEL spectra from the optical phonon polariton modes supported by silica, whose excitation probability is strongly influenced by the electron beam position. We have demonstrated the different spatial decay of the polaritonic signal compared to the nonpolaritonic contribution, which was not clarified in previous studies on vibrational EELS, and we discussed the possibility of distinguishing the material interface at high spatial resolution from the energy-filtered line scans. Although we studied specific material systems, our findings can be generalized and serve as an example for correct interpretation and analysis of experimental data from spatially resolved vibrational EELS in common experimental geometries.

## ACKNOWLEDGMENTS

A.K., R.H., and J.A. acknowledge the support of the Spanish Ministry of Economy, Industry and Competitiveness (national projects MAT2015-65525-R, FIS2016-80174-P, and project MDM-2016-0618 of the Maria de Maetzu Units of

Excellence Programme). A.K. further acknowledges Thermo Fisher Scientific and the Czechoslovak Microscopic Society scholarship for young researchers. P.A.C., K.V., and P.R. acknowledge support from the US National Science Foundation CHE-1508667 and the use of (S)TEM at John M. Cowley Center for High Resolution Electron Microscopy, Eyring Materials Center at Arizona State University.

#### APPENDIX A: EELS CALCULATIONS IN COMSOL MULTIPHYSICS

To perform EELS calculations, we utilize the radio-frequency (RF) toolbox in the frequency domain. We employ either 2D simulations, where Maxwell's equations are solved in  $(x, y, z)$  space, or the fully 3D simulation domain in real  $(x, y, z)$  space. The fast electron beam is implemented as an oscillating “edge current” in a 3D simulation domain and a “surface current” in a 2D simulation domain. The current is expressed as  $\mathbf{I} = \mathbf{I}_0 \exp(i\omega z/v)$  and applied along a straight line representing the beam trajectory. The EEL probability is evaluated from 3D calculations according to Eq. (2) directly with this software using an “edge probe” along the trajectory. All simulations are performed twice: with  $\varepsilon(\mathbf{r}, \omega)$  corresponding to the probed structure and then with  $\varepsilon(\mathbf{r}, \omega) = 1$  everywhere, so that only the field of the electron is present. Afterwards, the loss probability obtained from these two calculations is subtracted to correct for the finite length of the electron trajectory and nonzero values of the

fast electron field at the boundaries of the simulation domain [8,54,55].

#### APPENDIX B: EXPERIMENTAL DETAILS

A clean-room silicon wafer was thermally oxidized at 900 °C to obtain a  $\sim 3 \mu\text{m}$  surface-film of silica. Specimen preparation for STEM-EELS analysis involved performing a lift-out procedure on the oxidized wafer using a Nova 200 NanoLab (FEI) focused ion beam combined with a scanning electron microscope (SEM). The thickness of the lift-out specimen measured using SEM approached  $\sim 100 \text{ nm}$  near the edges and  $\sim 80 \text{ nm}$  near the silica-silicon interface. STEM-EELS analysis on the specimen was performed using a NION UltraSTEM 100 aberration-corrected microscope equipped with a monochromator, operated at 60 kV. The probe convergence semiangle was 28 mrad, and a 1 mm spectrometer entrance aperture was used corresponding to a collection semiangle of 12 mrad. During the monochromated experiment, the probe size was  $\sim 1.6 \text{ nm}$ , the beam current was  $\sim 10 \text{ pA}$ , and energy resolution was 16 meV. A dispersion of 1 or 2 meV per channel was used to record EEL spectra, which were subsequently calibrated and processed using the Gatan Microscopy Suite. The uncertainty in the energy position of a vibrational signal was the channel width, i.e.,  $\pm 1$  or  $\pm 2 \text{ meV}$ . For background subtraction, a power-law model of the form  $AE^{-r}$ , where  $E$  is the energy loss with  $A$  and  $r$  as constant parameters, was fitted to two 20 meV windows just before and after the vibrational signal [56].

- 
- [1] R. F. Egerton, *Electron Energy-Loss Spectroscopy in the Electron Microscope*, 3rd ed. (Springer, New York, 2011).
- [2] O. L. Krivanek, T. C. Lovejoy, N. Dellby, T. Aoki, R. W. Carpenter, P. Rez, E. Soignard, J. Zhu, P. E. Batson, M. J. Lagos, R. F. Egerton, and P. A. Crozier, *Nature (London)* **514**, 209 (2014).
- [3] P. Rez, T. Aoki, K. March, D. Gur, O. L. Krivanek, N. Dellby, T. C. Lovejoy, S. G. Wolf, and H. Cohen, *Nat. Commun.* **7**, 10945 (2016).
- [4] P. A. Crozier, T. Aoki, and Q. Liu, *Ultramicroscopy* **169**, 30 (2016).
- [5] D. M. Haiber and P. A. Crozier, *ACS Nano* **12**, 5463 (2018).
- [6] C. Dwyer, T. Aoki, P. Rez, S. L. Y. Chang, T. C. Lovejoy, and O. L. Krivanek, *Phys. Rev. Lett.* **117**, 256101 (2016).
- [7] M. J. Lagos, A. Trügler, U. Hohenester, and P. E. Batson, *Nature (London)* **543**, 529 (2017).
- [8] A. A. Goyadinov, A. Konečná, A. Chuvilin, S. Vélez, I. Dolado, A. Y. Nikitin, S. Lopatin, F. Casanova, L. E. Hueso, J. Aizpurua, and R. Hillenbrand, *Nat. Commun.* **8**, 95 (2017).
- [9] J. C. Idrobo, A. R. Lupini, T. Feng, R. R. Unocic, F. S. Walden, D. S. Gardiner, T. C. Lovejoy, N. Dellby, S. T. Pantelides, and O. L. Krivanek, *Phys. Rev. Lett.* **120**, 095901 (2018).
- [10] J. R. Jokisaari, J. A. Hachtel, X. Hu, A. Mukherjee, C. Wang, A. Konecna, T. C. Lovejoy, D. N., J. Aizpurua, O. L. Krivanek, J.-C. Idrobo, and R. F. Klie, *Adv. Mater.* **30**, 1802702 (2018).
- [11] P. Batson, N. Dellby, and O. Krivanek, *Nature (London)* **418**, 617 (2002).
- [12] P. Batson, *Nature (London)* **366**, 727 (1993).
- [13] F. J. García de Abajo, *Rev. Mod. Phys.* **82**, 209 (2010).
- [14] D. Muller and J. Silcox, *Ultramicroscopy* **59**, 195 (1995).
- [15] F. S. Hage, R. J. Nicholls, J. R. Yates, D. G. McCulloch, T. C. Lovejoy, N. Dellby, O. L. Krivanek, K. Refson, and Q. M. Ramasse, *Sci. Adv.* **4**, eaar7495 (2018).
- [16] R. J. Nicholls, F. S. Hage, D. G. McCulloch, Q. M. Ramasse, K. Refson, and J. R. Yates, *arXiv:1804.10475*.
- [17] H. Ibach and D. L. Mills, *Electron Energy Loss Spectroscopy and Surface Vibrations* (Academic, London, 1982).
- [18] P. Rez, *Microsc. Microanal.* **20**, 671 (2014).
- [19] C. Dwyer, *Phys. Rev. B* **89**, 054103 (2014).
- [20] C. Dwyer, *Phys. Rev. B* **96**, 224102 (2017).
- [21] K. Venkatraman, P. Rez, K. March, and P. A. Crozier, *Microscopy* **67**, i14 (2018).
- [22] R. Egerton, P. Li, and M. Malac, *Micron* **35**, 399 (2004).
- [23] R. Egerton, *Ultramicroscopy* **180**, 115 (2017).
- [24] J. D. Caldwell, L. Lindsay, V. Giannini, I. Vurgaftman, T. L. Reinecke, S. A. Maier, and O. J. Glembocki, *Nanophotonics* **4**, 44 (2015).
- [25] D. Basov, M. Fogler, and F. G. de Abajo, *Science* **354**, aag1992 (2016).
- [26] R. H. Ritchie, *Phys. Rev.* **106**, 874 (1957).
- [27] J. Nelayah, M. Kociak, O. Stéphan, F. J. G. de Abajo, M. Tencé, L. Henrard, D. Taverna, I. Pastoriza-Santos, L. M. Liz-Marzán, and C. Colliex, *Nat. Phys.* **3**, 348 (2007).

- [28] M. Couillard, A. Yurtsever, and D. A. Muller, *Phys. Rev. B* **77**, 085318 (2008).
- [29] H. Cohen, T. Maniv, R. Tenne, Y. Rosenfeld Hacoheh, O. Stephan, and C. Colliex, *Phys. Rev. Lett.* **80**, 782 (1998).
- [30] P. Moreau, N. Brun, C. A. Walsh, C. Colliex, and A. Howie, *Phys. Rev. B* **56**, 6774 (1997).
- [31] H. Lourenço-Martins and M. Kociak, *Phys. Rev. X* **7**, 041059 (2017).
- [32] A. Konečná, T. Neuman, J. Aizpurua, and R. Hillenbrand, *ACS Nano* **12**, 4775 (2018).
- [33] M. Morita, T. Ohmi, E. Hasegawa, M. Kawakami, and M. Ohwada, *J. Appl. Phys.* **68**, 1272 (1990).
- [34] D. A. Muller, T. Sorsch, S. Moccio, F. Baumann, K. Evans-Lutterodt, and G. Timp, *Nature (London)* **399**, 758 (1999).
- [35] A. Huber, J. Wittborn, and R. Hillenbrand, *Nanotechnology* **21**, 235702 (2010).
- [36] J. Aizpurua, A. Howie, and F. J. García de Abajo, *Phys. Rev. B* **60**, 11149 (1999).
- [37] J. Aizpurua, A. Howie, and F. J. García de Abajo, in *Electron Microscopy, Proceedings of the 14th International Congress on Electron Microscopy, Cancun, Mexico*, edited by H. Benavides and M. Yacamán (Institute of Physics Publ., Bristol, 1998), p. 697.
- [38] A. Rivacoba and N. Zabala, *New J. Phys.* **16**, 073048 (2014).
- [39] R. García-Molina, A. Gras-Marti, A. Howie, and R. H. Ritchie, *J. Phys. C* **18**, 5335 (1985).
- [40] A. A. Lucas and E. Kartheuser, *Phys. Rev. B* **1**, 3588 (1970).
- [41] J. Bolton and M. Chen, *Ultramicroscopy* **60**, 247 (1995).
- [42] E. Kröger, *Z. Phys.* **235**, 403 (1970).
- [43] U. Hohenester, A. Trügler, P. E. Batson, and M. J. Lagos, *Phys. Rev. B* **97**, 165418 (2018).
- [44] J. Kischkat, S. Peters, B. Gruska, M. Semtsiv, M. Chashnikova, M. Klinkmüller, O. Fedosenko, S. Machulik, A. Aleksandrova, G. Monastyrskiy *et al.*, *Appl. Opt.* **51**, 6789 (2012).
- [45] C. T. Kirk, *Phys. Rev. B* **38**, 1255 (1988).
- [46] M. K. Gunde, *Physica B* **292**, 286 (2000).
- [47] E. D. Palik, *Handbook of Optical Constants of Solids* (Academic, New York, 1998), Vol. 3.
- [48] K. L. Kliewer and R. Fuchs, *Phys. Rev.* **144**, 495 (1966).
- [49] A. A. Lucas, E. Kartheuser, and R. G. Badro, *Phys. Rev. B* **2**, 2488 (1970).
- [50] R. B. Pettit, J. Silcox, and R. Vincent, *Phys. Rev. B* **11**, 3116 (1975).
- [51] M. J. Lagos, A. Trügler, V. Amarasinghe, L. C. Feldman, U. Hohenester, and P. E. Batson, *Microscopy* **67**, i3 (2018).
- [52] Y. Li, M. Wu, N. Li, Y. Sun, C. Shi, X. Zhu, J. Guo, D. Yu, and P. Gao, [arXiv:1809.08615](https://arxiv.org/abs/1809.08615).
- [53] T. Lovejoy, G. Corbin, N. Dellby, M. Hoffman, and O. Krivanek, *Microsc. Microanal.* **24**, 446 (2018).
- [54] A. Wiener, H. Duan, M. Bosman, A. P. Horsfield, J. B. Pendry, J. K. W. Yang, S. A. Maier, and A. I. Fernández-Domínguez, *ACS Nano* **7**, 6287 (2013).
- [55] S. Raza, N. Stenger, A. Pors, T. Holmgaard, S. Kadkhodazadeh, J. B. Wagner, K. Pedersen, M. Wubs, S. I. Bozhevolnyi, and N. A. Mortensen, *Nat. Commun.* **5**, 5125 (2014).
- [56] J. A. Hachtel, A. R. Lupini, and J. C. Idrobo, *Sci. Rep.* **8**, 5637 (2018).